Regular Article

Synthesis, growth, optical and anisotropic mechanical behaviour of organic nonlinear optical imidazolium 2-chloro-4-nitrobenzoate single crystals

Varadharajan Krishnakumar[a], Jeyaram Jayaprakash, Singaram Boobas, and Muniraj Komathi

Department of Physics, Periyar University, Salem-636011, Tamil Nadu, India

Abstract. The title compound, imidazolium 2-chloro-4-nitrobenzoate (I2C4NB), has been synthesized and optical quality single crystals were grown with a dimension of $4 \times 2 \times 1 \, \mathrm{mm}^3$ using an ethanol and acetone (1:1) mixed solvent by slow evaporation solution growth technique. The powder XRD analysis confirmed the crystal structure and found that it is crystallized in the non-centrosymmetric space group $P2_1$ with the monoclinic system. The symmetries of molecular vibrations were confirmed by FT-IR spectrum. The CHN(S) analysis confirmed the stoichiometric composition of the grown crystal. It also exhibits a good transparency in the entire visible region (300–800 nm) and it was thermally stable up to $131.1\,^{\circ}\mathrm{C}$. The microhardness measurement shows the anisotropic nature of I2C4NB and also that it belongs to a soft material category. Photoconductivity studies reveal a linear increase of the photocurrent with respect to the applied electric field. HOMO LUMO studies were carried out for the crystal. The second harmonic generation test by the Kurtz powder method shows that the crystal exhibits phase matching and a conversion efficiency which is 2 times that of KDP.

1 Introduction

In modern times, nonlinear optical materials are the frontier of new science and technologies and have galvanized researchers to look for newer material with enhanced properties. Considerable attempts are being made to design new nonlinear optical (NLO) materials with improved second harmonic conversion efficiencies, as they are employed for a variety of applications, such as electro-optic modulation (EOM), optical information processing, laser frequency conversion, frequency mixing, terahertz (THz) wave generation, optical computing, 3D optical data storage, optical switching, photodynamic therapies and communication devices [1–5]. Inorganic materials are one step below in synthetic flexibility and hyperpolarizability with respect to organic materials [6]. The elementary structure of organic NLO materials relies on the π bond system; due to the delocalization of electronic charge distribution, overlap of π orbitals leads to a high mobility of the electron density. Functionalization of each end of the π bond system with proper acceptor and electron donor groups will enhance the asymmetric electronic distribution, which leads to a multiplied optical nonlinearity [7,8]. Non-centrosymmetric and highly hyperpolarizable materials can be attained either by attaching a proper substituent that causes a steric hindrance or by combining it with another molecule that has a favorable crystal structure [9]. Semiconductor laser diodes are now thought of as a prime candidate because of their potential advantage of compactness and low price. However, second harmonic generation (SHG) devices have a choice of wavelengths, advantages of emission power, and reliability, which make them fascinating for sensible applications. $KNbO_3$ is the best inorganic nonlinear optical material for frequency doubling in diode lasers [10]. In the development of the organic SHG device, some organic nonlinear materials have been studied, such as 3-methoxy-4-hydroxybenzaldehyde (MHBA) [11] and 8(4'-acetylphenyl)1,4-dioxa-8-azaspirol (APDA) [12]. Imidazole is an aromatic compound which consists of a lone pair nitrogen connected through a benzene ring and this lone pair nitrogen in imidazole favors the formation of salts with diverse organic and inorganic compounds. Imidazole ring as donor-acceptor–substituted stilbene to fabricate NLO materials has attracted wide attention as a result of its distinct optical properties of both linear and nonlinear optical natures [13–15]. However, the dipolar interactions of these organic chromophores tend to form a symmetrical structure, which brings strategic difficulties to fabricate a novel SHG material. It can be overcome

[a] e-mail: vkrishna_kumar@yahoo.com
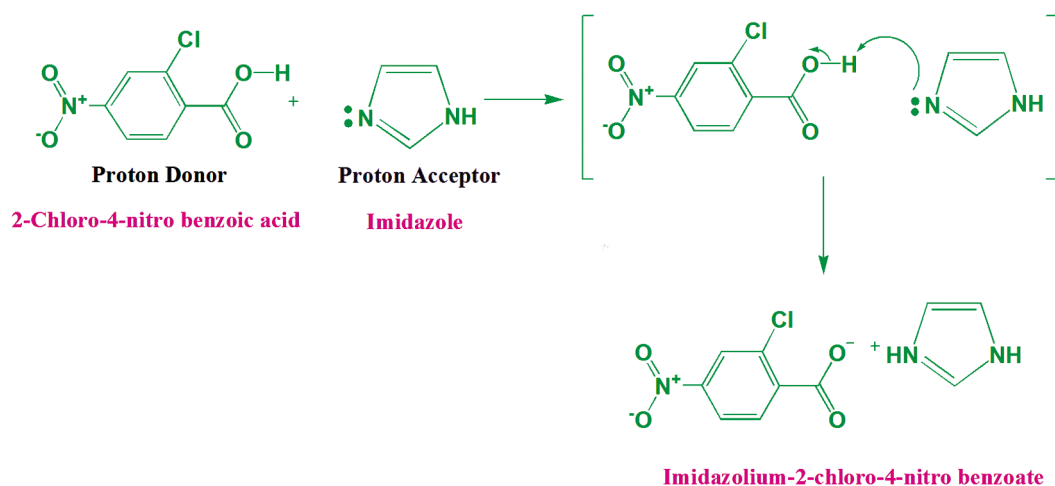
Fig. 1. Reaction mechanism for the imidazolium-2chloro-4-nitrobenzoate crystal.

by substituting the proton donor group with imidazole, which acts as a mediator for proton transfer reaction and forms a non-centrosymmetric structure [16–18]. Some of the reported promising NLO crystals of imidazole derivatives are imidazolium L-tartrate [19], imidazolium picrate [18], imidazole-imidazolium picrate monohydrate (IIP) [20], 1-ethyl-3-methyl imidazolium tribromoplumbate (EMITB) [21], benzil doped benzimidazole (BMZ) [22], benzimidazole [23] and benzimidazolium perchlorate [24]. The structure of imidazolium 2-chloro 4-nitrobenzate (I2C4NB) has been reported earlier [25] and it possesses the conjugated D-π-A bonds, which give a strong π-electron delocalization and their strong hydrogen bonding not only enhances the nonlinearity but it also improves the mechanical, chemical and thermal properties of the material. In the present paper, we present our investigations on synthesis, bulk growth, optical, thermal, elemental, mechanical and NLO properties of I2C4NB crystals.

2 Materials and methods

2.1 Synthesis

The reactants 2-chloro-4-nitrobenzoic acid and imidazole were commercially purchased (Merck, AR Grade > 99%) and used without any further purification. The I2C4NB was synthesized by taking an equimolar quantity of 2-chloro-4-nitrobenzoic acid and imidazole in an acetonitrile solvent. The starting materials were dissolved separately in the acetonitrile and the dissolved 2-chloro-4-nitrobenzoic acid solution was added dropwise to the imidazole solution [25]. In this case, protonation takes place between the amine and aromatic carboxylic acid; as a result, a short hydrogen bond N-H$\cdots$O held the benzoate and imidazolium ions together, which implies for the nitro and carboxyl groups to twist out of the benzene ring. By continuous stirring for 30 minutes, the resultant product was precipitated and it was purified by recrystallization using the mixed ethanol and acetone (1:1). The reaction mechanism is given in fig. 1.

2.2 Solubility

Selection of solvent plays a vital role in the growth of bulk single crystal because a different morphology of the same material can be obtained by growing it in different solvents. Therefore, before stepping into the growth process, the solubility of I2C4NB recrystallize powder was studied in different solvents, namely acetone, ethanol and mixed ethanol and acetone (1:1) at 30–50 °C with an interval of 5 °C. The saturated solutions of all three different solvents were prepared and kept in a thermostatically controlled water bath to ensure the uniformity in concentration and temperature. A small amount of solution was taken out and gravimetrically analyzed [26]; the same procedure was adopted for different temperatures and is shown in fig. 2. The solubility curve shows a positive slope, hence it is possible to grow the material by slow evaporation and slow cooling techniques.

2.3 Crystal growth

The saturated solution of I2C4NB in all three solvents was prepared at 30 °C and kept in a water bath, equipped with a temperature accuracy of ±0.01 °C. Prior to initiating the crystal growth, the bearing of any false nuclei present in
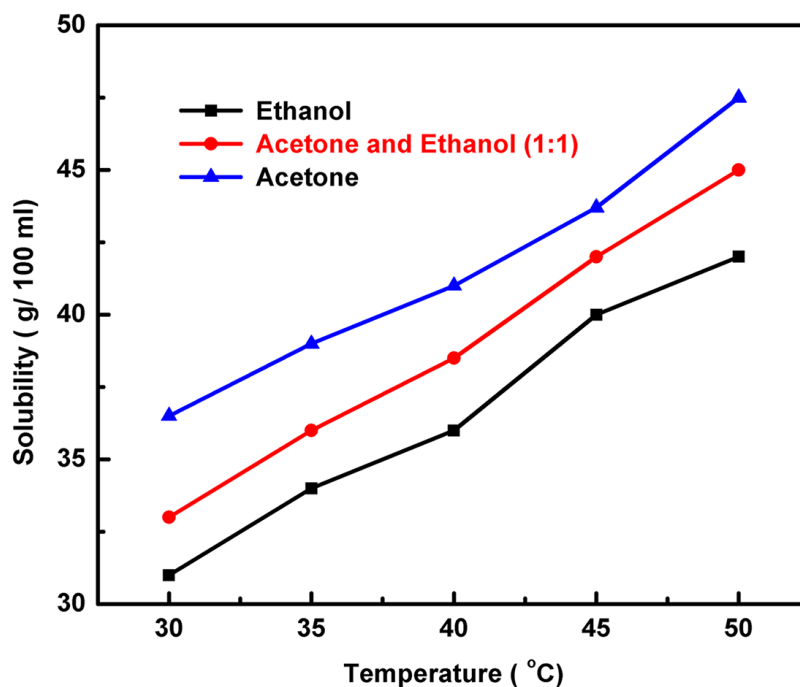
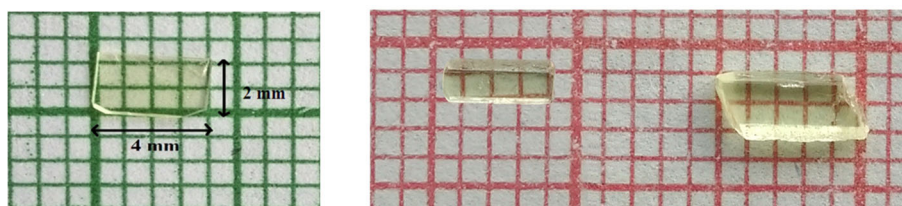**Fig. 2.** Solubility curve of I2C4NB for different solvents.

Fig. 3. Photograph of as-grown crystals.

the solution was dissolved by raising the temperature of the solution above the saturation temperature and holding it for 24 hours. The temperature of the solution was then slowly lowered to $30\,^{\circ}$C with a cooling rate of $0.2\,^{\circ}$C/h. After accomplishing the saturation temperature, the growth was performed by the isothermal solvent evaporation method. Needle-like and cluster crystals were formed in the acetone and ethanol solution, so it is not possible to grow bulk crystals in these solvents. High-quality bulk single crystals of I2C4NB were obtained in the mixed solvent after 15 days with a dimension of $4 \times 2 \times 1\,\text{mm}^3$. The as-grown single crystals of I2C4NB are shown in fig. 3.

3 Result and discussion

3.1 X-ray diffraction analysis

In order to confirm the phase formation of the I2C4NB crystal, the powder XRD pattern was recorded for the grown sample in the 2θ range 10° to 50° using Rigaku Miniflex-II X-ray diffractometer equipped with Cu Kα ($\lambda = 1.54\,\text{Å}$) radiation operating at $40\,\text{kV}$ with $30\,\text{mA}$. Figure 4 shows the simulated and experimental powder XRD pattern of the I2C4NB single crystal grown from the mixed ethanol and acetone (1:1) solution. The powdered diffraction pattern of the already reported crystal was simulated in mercury software by making use of the CIF file [25]. The powdered diffraction pattern reveals the structure and crystallinity of the grown crystal and the simulated pattern coincides with experimental one with varied intensities. The material is crystallized in monoclinic crystal system with a non-centrosymmetric space group P2$_1$. The lattice parameters of the grown crystal were performed using the 2θ and its indexed $h\,k\,l$ values. The calculated lattice parameter of the grown single crystal is in good agreement with the earlier reports [25] and is given in table 1.
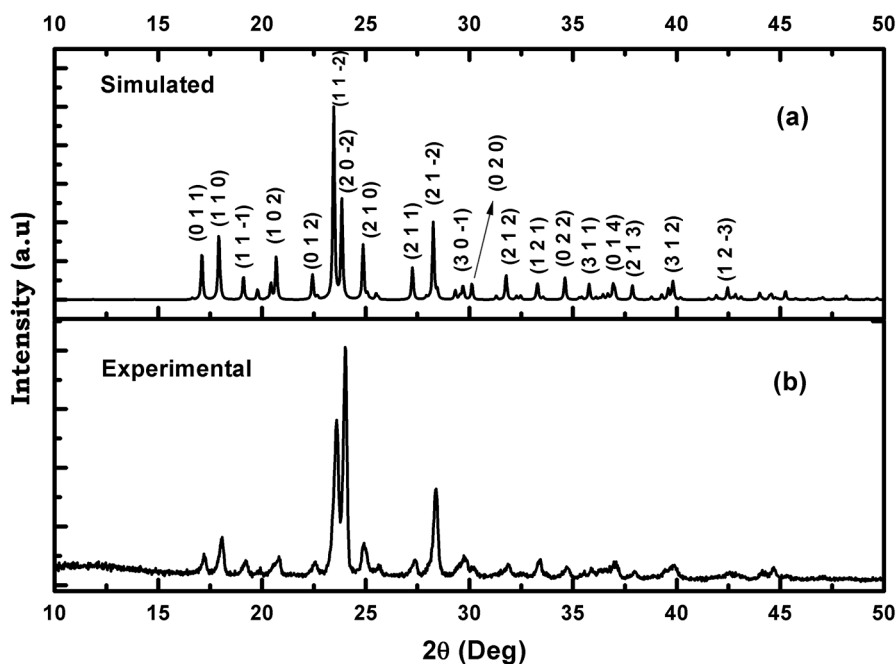
Fig. 4. Powdered XRD pattern of I2C4NB crystal: (a) simulated and (b) experimental.

Table 1. XRD data of the I2C4NB crystal.

Category	Crystal system	Space group	Volume (Å)^3	Cell parameters (Å)
Reported	Monoclinic	P2$_1$	572.507	$a = 09.078$
				$b = 05.928$
				$c = 10.771$
Grown	Monoclinic	P2$_1$	575.628	$a = 09.053$
				$b = 05.918$
				$c = 10.749$

3.2 FTIR analysis

The Fourier transform infrared (FTIR) spectra were recorded at room temperature using Brucker Tensor - 27 spectrophotometer with a resolution of $2\,cm^{-1}$ in the range 4000–$400\,cm^{-1}$ following the KBr pellet technique and is shown in fig. 5. The formation of the I2C4NB complex was evidenced by the presence of characteristic bands of N-H, NO$_2$ and COO$^-$, respectively. It is evident from the spectrum that the strong wideband at $3155\,cm^{-1}$ is due to the N-H stretching vibration. The vibration bands at 3110 and $2494\,cm^{-1}$ are due to aromatic C-H asymmetric and symmetric stretching vibrations. The asymmetric and symmetric stretching vibrations of carboxylate anion COO$^-$ are observed at 1591 and $1398\,cm^{-1}$, respectively. The peaks at 1519 and $1352\,cm^{-1}$ are due to symmetric and asymmetric vibrations of the NO$_2$ aromatic nitro group. The bands at 1216, 1043 and $930\,cm^{-1}$ are due to C-N asymmetric and symmetric stretching vibrations. The C-H in plane and out-of-plane bending vibrations appear at 1182 and $815\,cm^{-1}$, respectively. The C-C out-of-plane bending is observed at $865\,cm^{-1}$. The presence of carbon and chloride bond is confirmed by the absorption peak at $746\,cm^{-1}$. The N-H plane bending vibration appears at $665\,cm^{-1}$. The observed peaks at 633, 553 and $512\,cm^{-1}$ are due to the bending, wagging and rocking vibrations of the carboxylate anion present in the material [27–30]. The frequency assignments for the crystal I2C4NB are shown in table 2.

3.3 Elemental analysis

The elemental analysis of the I2C4NB crystal was performed using the LECO Truspec CHN(S) analyzer and the values are given in table 3. The observed experimental value of carbon, hydrogen and nitrogen are 44.17%, 2.81%, and 15.19%, respectively. The observed values are in good agreement with the calculated theoretical values of carbon (44.54%), hydrogen (2.99%) and nitrogen (15.58%), respectively. Thus, the expected elements in the I2C4NB crystal were confirmed.

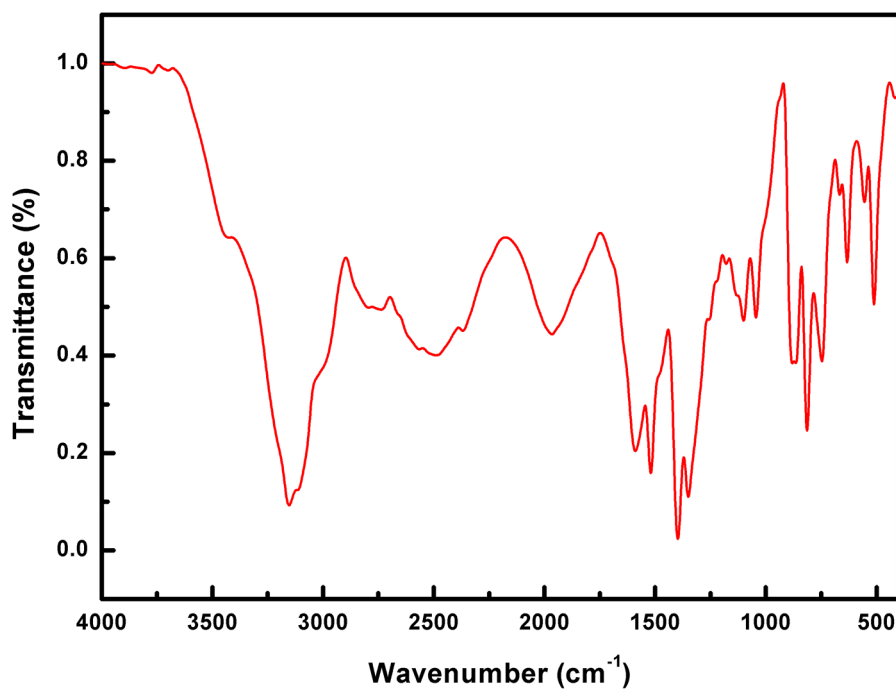**Fig. 5.** FTIR spectrum of the I2C4NB crystal.

Table 2. FTIR frequency assignments.

Wavenumber (cm^{-1})	Assignments
3155	N-H stretching vibration
3110	Aromatic C-H asymmetric stretching vibration
2494	Aromatic C-H symmetric stretching vibration
1591	COO$^-$ asymmetric stretching vibration of carboxylate anion
1398	COO$^-$ symmetric stretching vibration of carboxylate anion
1519	NO$_2$ asymmetric stretching vibration
1352	NO$_2$ symmetric stretching vibration
1216, 1043 and 930	C-N asymmetric and symmetric vibrations
1182, 815	C-H in plane and out of plane bending vibration
865	C-C out of plane bending vibration
746	C-Cl stretching vibration
665	N-H plane bending vibration
633	COO$^-$ bending
553	COO$^-$ wagging
512	COO$^-$ rocking

Table 3. Microanalysis of the I2C4NB crystal.

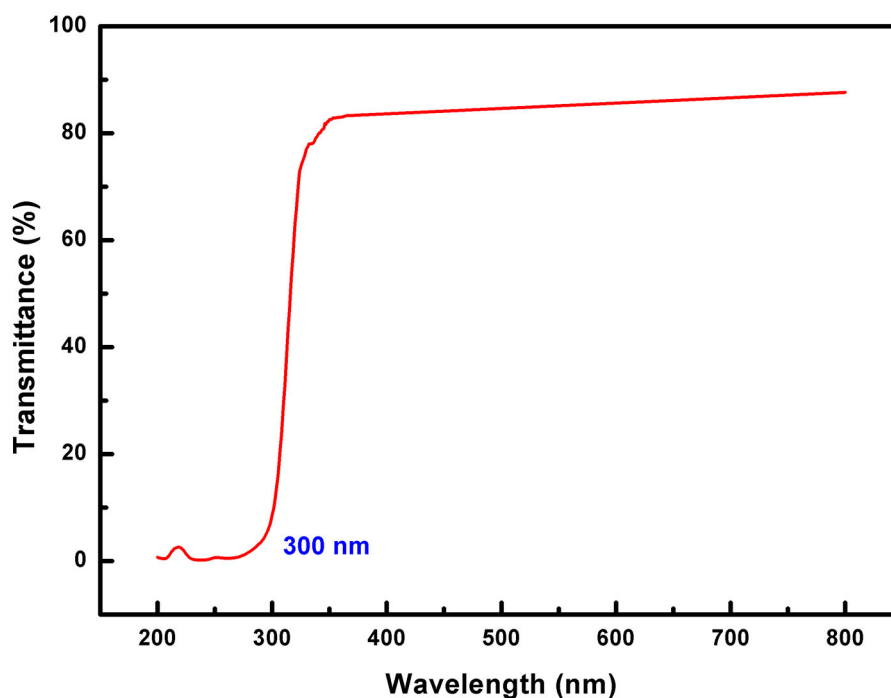| S. No	Element	Theoretical (%)	Experimental (%)
1	C	44.54	44.17
2	H	2.99	2.81
3	N	15.58	15.19

Fig. 6. UV-Vis transmittance spectrum of the I2C4NB crystal.

3.4 UV-Vis spectroscopy

To determine the transmission range and hence to know the suitability of I2C4NB single crystals for optical applications, the optical transmittance spectrum of the I2C4NB single crystal was recorded by using JASCO spectrophotometer in the range 200–800 nm and is shown in fig. 6. The I2C4NB single crystal possessing a cut-off wavelength of 300 nm [21,22,24] with maximum (85%) transmission window (300 to 800 nm) is highly suitable for the generation of second harmonic light ($\lambda = 532$ nm) as well as third harmonic generation ($\lambda = 354.6$ nm) from the Nd: YAG laser ($\lambda = 1064$ nm) [17,27,31].

3.5 Thermal analysis

Thermal analysis for the grown crystal was performed using the Perkin Elmer Diamond TG/DTA analyzer in the nitrogen atmosphere from 30 °C to 450 °C at a heating rate of 10 °C/min to study its thermal stability and melting point. The simultaneous TG-DTA was performed on 8 mg of I2C4NB powder sample and the results are shown in fig. 7. In the DTA spectrum, it is observed that there is a sharp endothermic peak at 131.1 °C, which corresponds to the melting point of the compound. The absence of any characteristic endothermic or exothermic peak before this melting point confirms the absence of the isomorphic transition. The sharpness of the endothermic peak evidences the good degree of crystallinity of I2C4NB. The flat response of TG curve up to 162 °C confirms the non-existence of crystallization solvent or impurity in the crystal and most specifically the thermal stability of I2C4NB up to the onset of melting. The shape of the TG curve after its melting represents the thermal decomposition of I2C4NB with the formation of volatile reaction products [32]. The single stage complete mass loss from 162 to 291 °C illustrates the decomposition of the grown crystal and the removal of almost all fragments as gaseous products. The decomposition temperature T_d was identified as 291 °C, which was estimated as the temperature at the intercept of the leading edge of the mass loss that can involve sublimation and/or decomposition by the base line of the TG scans [33]. The TG-DTA plots clearly show that the title compound is thermally stable up to 131.1 °C. Further, it is important to note that the compound exhibited no phase transition until the material reaches its melting point. The melting point of I2C4NB obtained by the melting point apparatus is about 132 °C. The melting and decomposition points are very different, so we can grow the material by the melt technique for further device fabrications.

3.6 Microhardness study

The mechanical behaviour of pure I2C4NB crystal was investigated by applying loads of 25, 50 and 100 g, using the Shimadzu HMV-2 microhardness analyzer. For the (001) and (100) planes, several indentations were made on its
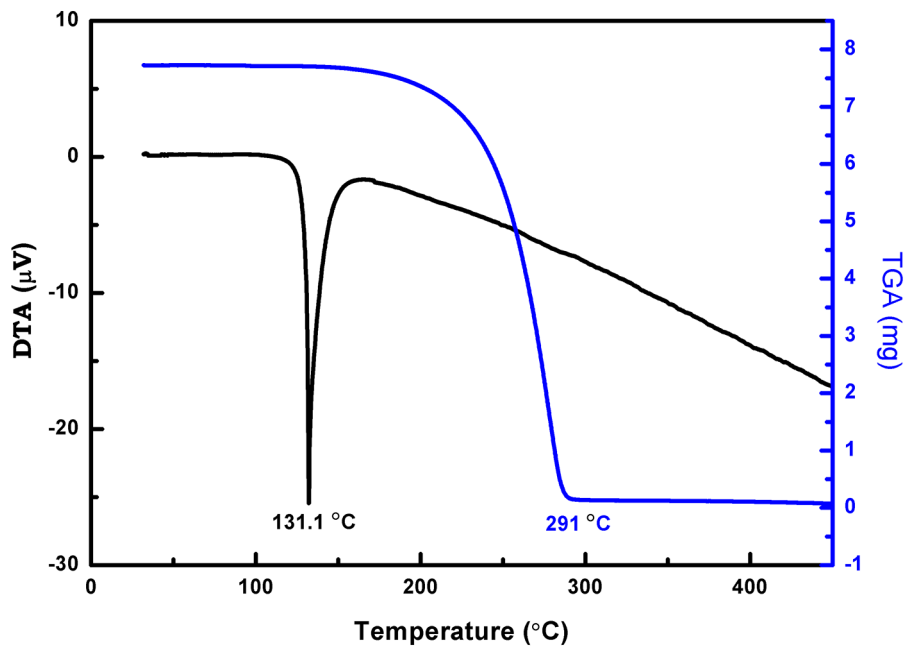
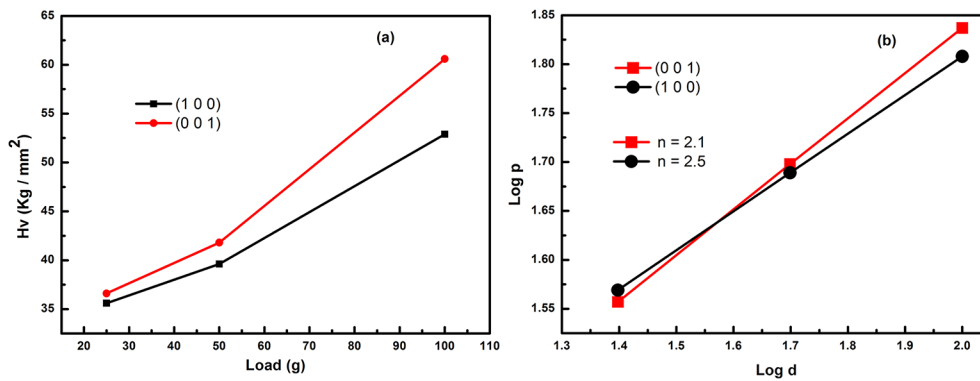**Fig. 7.** TG/DTA curve of the I2C4NB crystal.

Fig. 8. (a) Load-dependent hardness; (b) $\log P$ *vs.* $\log d$.

surface for the constant period of 10 s and the diagonal indentation length was recorded for each load. The vicker's hardness number H_v is calculated by using the following relation:

$$H_\mathrm{v} = 1.8554 \left(\frac{p}{d^2} \right) \ (\text{kg mm}^{-2}),$$

where d is the diagonal length of the impression in mm and P is the applied load in Kg. As a function of the applied load (P), the change in the microhardness value H_v and the plot of "$\log d$" *vs.* "$\log P$" are shown in figs. 8(a) and (b), respectively. Further, it is clear that the microhardness value increases for an increase of the load for both planes and it is in agreement with the reverse indentation size effect (RISE). Due to the release of the internal stress generated by indentation, micro cracks were observed above 100 g of a load. The slope of the "$\log P$" *vs.* "$\log d$" gives the straight line for both orientations. The Mayer's number (n) for the grown I2C4NB crystal is calculated using the relation

$$P = 1.854 \, K d^n.$$

Here, "n" is Meyer's index or work hardening coefficient that has been determined from the slope of a straight line using the least square fit method. The calculated n values of the I2C4NB single crystal along different crystallographic orientations are listed in table 4. According to Onitsch and Hannman [34–36] n should lie between 1 to 1.6 for hard materials and above 1.6 for soft materials. From the calculated n values of the I2C4NB single crystal along various orientations, it could be observed that the measured orientations exhibit soft material behaviour, obeying RISE and also anisotropic in nature, since the hardness depends on the orientation of the crystal. A similar anisotropic

Table 4. Anisotropic hardness behaviour of the I2C4NB single crystal.

Orientation	Hardness number H_v for a load of			Work hardness co-efficient n
	25 (g)	50 (g)	100 (g)	
1 0 0	33.6	39.6	52.9	2.52
0 0 1	36.6	41.8	60.6	2.16
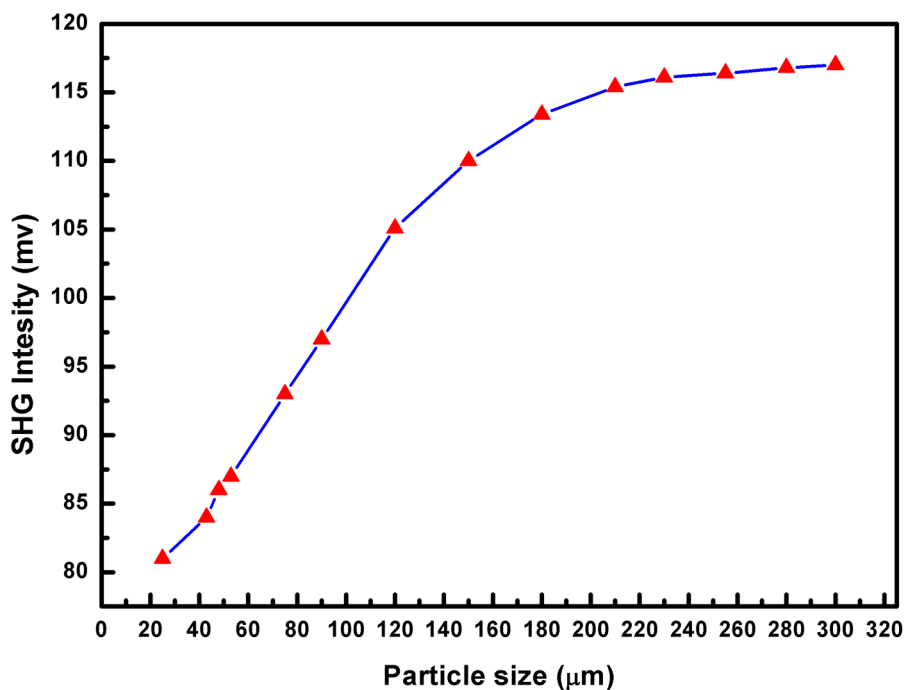
Fig. 9. Particle size dependence SHG output of the I2C4NB crystal.

nature was observed for other NLO crystals, such as bis(thiourea) cadmium chloride [37], cesium hydrogen L-malate monohydrate [38], sodium p-nitrophenolate dihydrate [39], with respect to constant load and, similarly, with respect to different loads, a similar nature was also observed for few other NLO crystals, such as imidazole-imidazolium picrate monohydrate (IIP) [20], ammonium malate [40], urea L-malic acid [41], piperidinium p-hydroxybenzoate [42], hydrazonium L-tartrate [43] and β-cyclotetramethylene-tetranitramine [44]. For the I2C4NB crystal the hardness value for the (001) plane is higher than for the (100) plane. The intermolecular and intramolecular bonding is responsible for the variation of hardness value in different crystallographic orientations [39].

3.7 Nonlinear optical studies

The second harmonic generation of the grown sample was confirmed by the powder Kurtz method. The Q-switched Nd: YAG laser of wavelength 1064 nm with an input power of 5 mJ and pulses of 8 ns with a repetition rate of 10 Hz was used and the emitted SHG radiations of 532 nm were collected by a photomultiplier tube and then converted into the voltage at the CRO [45]. The particle size of the powdered crystalline sample decides the efficiency of second-order nonlinearity [46] so we sieved the crystalline powder into different particle size ranges: below 25, 25–43, 43–48, 40–53, 53–75, 75–90, 90–120, 120–150, 150–180, 180–210, 210–230, 230–255, 255–280 and 280–300 μm. When the powder sample of different sizes of I2C4NB was illuminated with this laser source, emission of green light (532 nm) was observed and its efficiency was found to increase with the increase of particle size and also it shows the phase matching ability of the material. The SHG conversion efficiency of I2C4NB is found to be 0.9 times that of urea and 2 times that of standard KDP. The SHG efficiency of I2C4NB for different particle ranges is shown in fig. 9.

3.8 Photoconductivity

Photoconductivity measurements for the grown I2C4NB crystals were taken using the Keithley electrometer (Model 6517B). Dark and photocurrent measurements on these crystals were carried out by the two probe technique at room
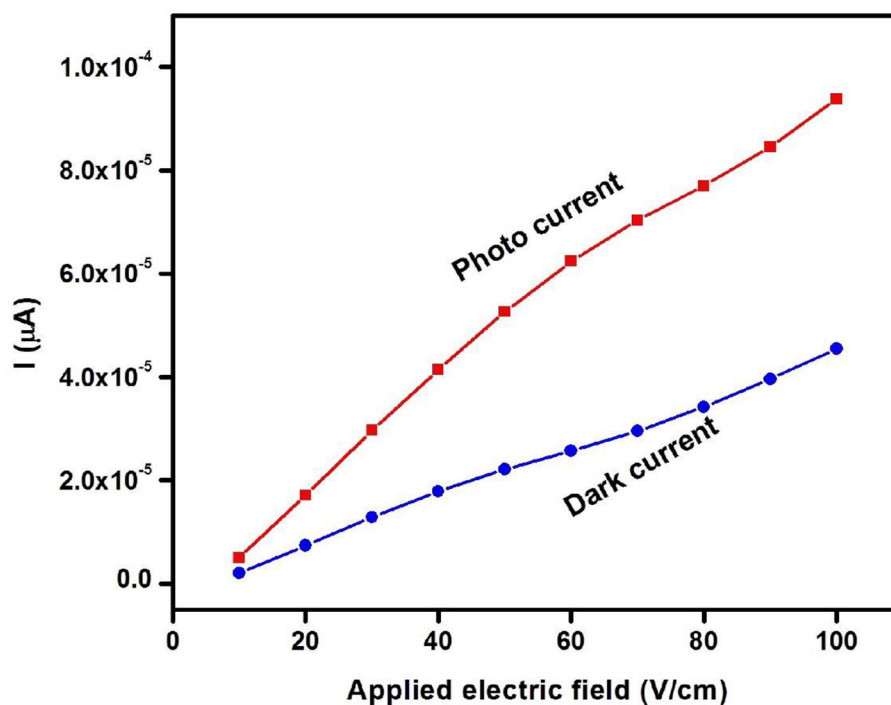
Fig. 10. Dark current and photocurrent response of the I2C4NB crystal.

Table 5. HOMO, LUMO, energy gaps and related molecular properties of the I2C4NB crystal (eV).

Molecular properties	B3LYP/6-311G
E_{HOMO} (eV)	-0.19435
E_{LUMO} (eV)	0.04722
Energy gap ($E_{\text{HOMO}} - E_{\text{LUMO}}$)	0.14713
Ionization energy (IE) $= -E_{\text{HOMO}}$	0.19435
Electron affinity (EA) $= -E_{\text{LUMO}}$	-0.04722
Global hardness (η) $= 1/2\,(E_{\text{HOMO}} - E_{\text{LUMO}})$	0.120785
Softness (S) $= 1/\eta$	4.139587
Mulliken electronegativity (χ)	0.073565
Global electrophilicity (ω) $= \mu^2/2\,\eta$	0.02240

temperature. Parallel faces of the crystals were coated with an electronic grade silver paint and a small copper wire was fixed on both sides of the sample. The sample was then connected in series to a DC power supply and electrometer. For dark current measurements the sample was protected from all the radiations and the input applied voltage was increased from 10 V to 100 V in steps of 10 V. The corresponding dark current was recorded. For photocurrent measurements, illumination from 100 W halogen lamp containing iodine vapour and a tungsten filament was used. Figure 10 shows the dark current and photocurrent response for the I2C4NB crystal. From the figure, it is clear that dark and photo currents are linear with applied input voltage and the photocurrent is higher than the dark current, which is termed as positive photoconductivity. It may be due to the increase of charge carriers in the presence of illumination. Materials with a positive photoconductivity nature can be used towards soliton wave communications [47].

3.9 FMO analysis

The B3LYP/6-311G method has been employed to compute the chemical parameters, *viz.* molecular orbital (HOMO and LUMO) energies, energy gap (ΔE) electron affinity (EA), ionization potential (IP), hardness (η), softness (S), absolute electronegativity (χ) and electrophilicity index (ω) as shown in table 5. The frontier orbital gap helps characterize the chemical reactivity and kinetic stability of the molecule. The HOMO is the orbital that mainly acts as an electron donor and the LUMO is the orbital that mainly acts as an electron acceptor. The energy gap HOMO
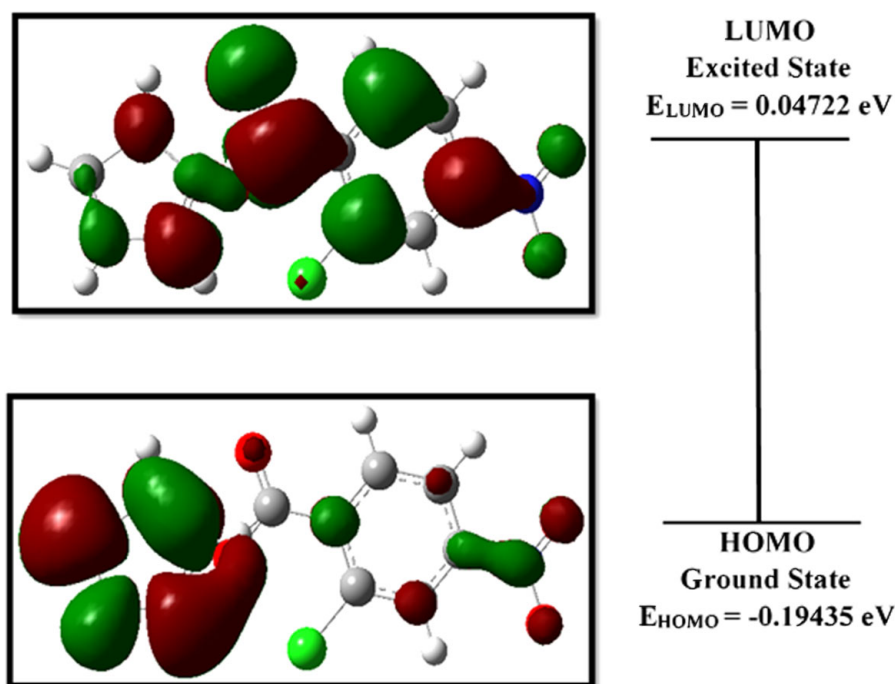
Fig. 11. FMO analysis of I2C4NB.

$(-0.19435\,\mathrm{eV})$ to LUMO $(0.04722\,\mathrm{eV})$ of the molecule is about $0.14713\,\mathrm{eV}$ and it is shown in fig. 11. The HOMO and LUMO energy explains the eventual charge transfer interactions taking place within the molecule and it also increases the polarizability of the molecule [48,49]. The calculated HOMO-LUMO energy gap value was compared with few of the know NLO single crystals, such as melaminium benzoate dehydrate [50], piperidinium p-hydroxybenzoate [51], pyrrolidinium p-hydroxybenzoate [52], and it possess less energy gap, which implies that I2C4NB has less energy barriers to transfer electrons between the occupied and unoccupied orbitals. The electrophilicity is a significant parameter, which is a measure of the molecule to accept the electrons. Nucleophilicity is an index of the molecule to donate the electrons. Thus, the electrophilicity and nucleophilicity of a molecule influence the electronic properties of the molecule. The molecule with higher electrophilicity values will be a poor donor, whereas the molecule having higher nucleophilicity will function as good donor. Thus, the reactivity of molecules and atoms is directly related to the ionization potential. But the softness and hardness of molecules give information about stability in addition to the reactivity [48].

4 Conclusion

An organic NLO compound I2C4NB has been synthesized and optical quality single crystals were grown using the slow evaporation solution growth method. I2C4NB was found to crystallize in the non-centrosymmetric space group of $\mathrm{P2}_1$. The presence of functional groups was confirmed by FTIR analysis. The presence of different elements was confirmed by the CHN(S) analyser. The transmission spectrum shows that the material can be used for the frequency conversion process in the 300–800 nm region. The TG-DTA studies revealed that the title compound has a good thermal stability and it could be used for optical applications below its melting point (131.1 °C). The mechanical hardness of the I2C4NB crystal was evaluated using the Vickers microhardness test and it confirmed that it exhibited soft material category and anisotropic behaviour, which were attributed to the nature and strength of the bonding environment in the measured orientations. The low value of the HOMO LUMO energy gap supports the charge transfer through π-conjugated system from donor to acceptor in the I2C4NB crystal. The photoconductivity investigation shows the positive photoconduction for the 12C4NB crystal. Further, the NLO measurement shows that the material is phase matchable and its conversion efficiency is two times that of standard KDP. The present investigation showed that the I2C4NB crystal could be a suitable candidate for NLO applications.

References

1. J. Chengmin, C. Tianliang, S. Zhihua, G. Yan, L. Wenxiong, L. Junhua, Q. Shi, H. Maochun, Cryst. Eng. Comm. **15**, 2157 (2013).
2. R. Surekha, R. Gunaseelan, P. Sagayaraj, K. Ambujam, Cryst. Eng. Comm. **16**, 7979 (2014).
3. K. Nivetha, S. Kalainathan, M. Yamada, Y. Kondo, F. Hamada, RSC Adv. **6**, 35977 (2016).
4. K. Anuj, N. Vijayan, S. Gupta, K. Thukral, V. Jayaramakrishnan, B. Singh, J. Philip, S. Das, K.K. Maurya G. Bhagavannarayana, RSC Adv. **4**, 56188 (2014).
5. K. Senthil, S. Kalainathan, A. Ruban Kumar, P.G. Aravindan, RSC Adv. **4**, 56112 (2014).
6. S. Ponnuswamy, V. Mohanraj, S. Ilango, M. Thenmozhi, M.N. Ponnuswamy, J. Mol. Struct. **1081**, 449 (2014).
7. R.N. Rai, K.B.R. Varma, J. Cryst. Growth **285**, 111 (2005).
8. V. Crasta, V. Ravindrachary, S. Lakshmi, S.N. Pramod, M.A. Shridar, J. Shashidhara Prasad, J. Cryst. Growth **275**, e329 (2005).
9. K. Jain, G.H. Hewig, Y.Y. Cheng, J.I. Crowley, IEEE J. Quant. Electron. **QE-17**, 1593 (1981).
10. G.T. Forrest, Laser Focus World **26**, 46 (1990).
11. M.H. Jiang, Bull. Chin. Ceram. Soc. **4**, 82 (1995).
12. M. Sagawa, H. Kagawa, A. Kakuta, Appl. Phys. Lett. **66**, 547 (1995).
13. J. Santos, E.A. Mintz, O. Zehnder, C. Bosshard, X.R. Bu, P. Gunter, Tetrahedron Lett. **42**, 805 (2001).
14. X.R. Bu, H. Li, D. VanDer Veer, E. Mintz, Tetrahedron Lett. **37**, 7331 (1996).
15. A. Carella, R. Centore, A. Fort, A. Peluso, A. Sirigu, A. Tuzi, Eur. J. Org. Chem. **12**, 2620 (2004).
16. W. Wu, R. Tang, Q. Li, Z. Li, Chem. Soc. Rev. **44**, 3997 (2015).
17. C. Ji, T. Chen, Z. Sun, Y. Ge, W. Lin, J. Luo, Q. Shi, M. Hong, Cryst. Eng. Comm. **15**, 2157 (2013).
18. S. Anandhi, T.S. Shyju, T.P. Srinivasan, R. Gopalakrishnan, J. Cryst. Growth **335**, 75 (2011).
19. K. Meena, K. Muthu, V. Meenatchi, M. Rajasekar, G. Bhagavannarayana, S.P. Meenakshi sundaram, Spectrochim. Acta A: Mol. Biomol. Spectrosc. **124**, 663 (2014).
20. P. Vivek, P. Murugakoothan, Opt. Laser Tech. **49**, 288 (2013).
21. T. Chen, Z. Sun, J.P. Niu, Q.G. Zhai, C. Jin, S. Wang, L. Li, Y. Wang, J. Luo, M. Hong, J. Cryst. Growth **325**, 55 (2011).
22. R. Ramesh Babu, M. Sukumar, V. Vasudevan, Mohd. Shakir, K. Ramamurthi, G. Bhagavannarayana, Mater. Res. Bull. **45**, 1194 (2010).
23. N. Vijayan, G. Bhagavannarayana, R. Ramesh Babu, R. Gopalakrishnan, K.K. Maurya, P. Ramasamy, Cryst. Growth Des. **6**, 1542 (2006).
24. L. Mariappana, A. Kandasamy, M. Rathnakumari, P. Suresh kumar, Optik **124**, 5707 (2013).
25. I. Hiroyuki, R. Bilkish, K. Setsuo, Acta Crystallogr. E **57**, 0744 (2001).
26. H. Joel, E.T. Hildebrand, C.W. Ellefson, J. Beebe, J. Am. Chem. Soc. **39**, 2301 (1917).
27. L. Chandra, J. Chandrasekaran, K. Perumal, B. Babu, Optik **127**, 3206 (2016).
28. C. Song, Y. Zhou, Z. Sun, T. Chen, S. Zhang, J. Luo, Cryst. Res. Technol. **50**, 866 (2015).
29. L. Wang, G. Zhang, X. Liu, X. Wang, L. Wang, L. Zhu, D. Xu, Cryst. Res. Technol. **48**, 1086 (2015).
30. R. Mani, I.B. Rietveld, B. Nicolaï, K. Varadharajan, M.L. Kultanen, N. Surumbarkuzhali, Chem. Phys. **458**, 52 (2015).
31. S. Gowri, T. Uma Devi, D. Sajan, C. SurendraDilip, A. Chandramohan, N. Lawrence, Spectrochim. Acta A: Mol. Biomol. Spectrosc. **110**, 28 (2013).
32. G. Shanmugam, K. Ravi Kumar, B. Sridhar, S. Brahadeeswaran, Mater. Res. Bull. **47**, 2315 (2012).
33. R. Bottom, *Thermogravimetric Analysis*, in *Principles and Applications of Thermal Analysis* (Blackwell, UK, 2008).
34. E.M. Onitsch, *Over the Microhardness of the Metals*, in *Mikroskopie*, Vol. **2** (1947) pp. 131–151.
35. E.M. Onitsch, *The Present Status of Testing the Hardness of Materials*, in *Mikroskopie*, Vol. **95** (1956) pp. 12–14.
36. M. Hanneman, Metall. Manchu. **23**, 135 (1941).
37. V. Venkataramanan, S. Maheswaran, J.N. Sherwood, H.L. Bhat, J. Cryst. Growth **179**, 605 (1997).
38. J.N. Babu Reddy, S. Vanishri, Ganesh Kamath, Suja Elizabeth, H.L. Bhat, D. Isakov, M. Belsley, E. de Matos Gomes, T.L. Aroso, J. Cryst. Growth **311**, 4044 (2009).
39. S. Brahadeeswaran, H.L. Bhat, N.S. Kini, A.M. Umarji, P. Balaya, P.S. Goyal, J. Appl. Phys. **88**, 5935 (2000).
40. G. Anandha Babu, P. Ramasamy, Curr. Appl. Phys. **10**, 214 (2010).
41. S. Vanishri, H.L. Bhat, A. Deepthy, V.P.N. Nampoori, E.D.M. Gomes, M. Belsley, J. Appl. Phys. **99**, 083107 (2006).
42. G. Shanmugam, K. Thirupugalmani, R. Rakhikrishna, J. Philip, S. Brahadeeswaran, J. Therm. Anal. Calorim. **114**, 1245 (2013).
43. V. Kannan, R. Rakhikrishnan, J. Philip, S. Brahadeeswaran, J. Therm. Anal. Calorim. **116**, 339 (2014).
44. H.G. Gallagher, J.C. Miller, D.B. Sheen, J.N. Sherwood, R.M. Vrcelj, Chem. Cent. J. **9**, 22 (2015).
45. S.K. Kurtz, T.T. Perry, J. Appl. Phys. **39**, 3798 (1968).
46. Y. Porter, K. Min Ok, N.S.P. Bhuvanesh, P.S. Halasyamani, Chem. Mater. **13**, 1910 (2001).
47. B. Milton Boaz, S. Mary Navis Priya, J. Mary Linet, P. Martin Deva Prasath, S. Jerome Das, Opt. Mater. **29**, 827 (2007).
48. T.W. Panunto, Z. Urbanczyk-Lipkowska, R. Johnson, M.C. Etter, J. Am. Chem. Soc. **109**, 7786 (1987).
49. M.C. Etter, P.W. Baures, J. Am. Chem. Soc. **110**, 639 (1988).
50. N. Kanagathara, M.K. Marchewka, M. Drozd, S. Gunasekaran, P.R. Rajakumar, G. Anbalagan, Spectrochim. Acta A: Mol. Biomol. Spectrosc. **145**, 394 (2015).
51. G. Shanmugam, K. Thirupugalmani, V. Kannan, S. Brahadeeswaran, Spectrochim. Acta A: Mol. Biomol. Spectrosc. **106**, 175 (2013).
52. G. Shanmugam, M.S. Belsley, D. Isakov, E. de Matos Gomes, K. Nehru, S. Brahadeeswaran, Spectrochim. Acta A: Mol. Biomol. Spectrosc. **114**, 184 (2013).